Article

Resolving molecular diffusion and aggregation of antibody proteins with megahertz X-ray free-electron laser pulses

Mario Reiser [1] ✉, Anita Girelli[2], Anastasia Ragulskaya[2], Sudipta Das[1], Sharon Berkowicz[1], Maddalena Bin [1], Marjorie Ladd-Parada [1], Mariia Filianina [1], Hanna-Friederike Poggemann[1,2], Nafisa Begam[2], Mohammad Sayed Akhundzadeh[3], Sonja Timmermann [3], Lisa Randolph [3], Yuriy Chushkin[4], Tilo Seydel [5], Ulrike Boesenberg[6], Jörg Hallmann[6], Johannes Möller[6], Angel Rodriguez-Fernandez [6], Robert Rosca[6], Robert Schaffer[6], Markus Scholz [6], Roman Shayduk[6], Alexey Zozulya [6], Anders Madsen [6], Frank Schreiber [2], Fajun Zhang[2], Fivos Perakis [1] ✉ & Christian Gutt [3] ✉

X-ray free-electron lasers (XFELs) with megahertz repetition rate can provide novel insights into structural dynamics of biological macromolecule solutions. However, very high dose rates can lead to beam-induced dynamics and structural changes due to radiation damage. Here, we probe the dynamics of dense antibody protein (Ig-PEG) solutions using megahertz X-ray photon correlation spectroscopy (MHz-XPCS) at the European XFEL. By varying the total dose and dose rate, we identify a regime for measuring the motion of proteins in their first coordination shell, quantify XFEL-induced effects such as driven motion, and map out the extent of agglomeration dynamics. The results indicate that for average dose rates below 1.06 kGy μs^{-1} in a time window up to 10 μs, it is possible to capture the protein dynamics before the onset of beam induced aggregation. We refer to this approach as *correlation before aggregation* and demonstrate that MHz-XPCS bridges an important spatio-temporal gap in measurement techniques for biological samples.

The European X-ray Free-Electron Laser Facility (EuXFEL) is the first X-ray free electron laser (XFEL) generating ultrashort hard X-ray pulses with megahertz repetition rate. Megahertz X-ray photon correlation spectroscopy (MHz-XPCS)[1–3] makes use of this high repetition rate and the high degree of transverse coherence to measure diffusive dynamics with (sub-) microsecond temporal resolution. In biological systems, typical diffusion coefficients in dense cellular environments range from $D_0 \approx 0.1$ to 10 nm^2 μs^{-1}[4–9] which requires to resolve time scales from $\tau \approx 0.5$ to 5 μs (see Fig. 1) in order to trace the complex many-body interactions between proteins and the solvent on molecular length scales. This window of length and time scales is not accessible by optical techniques such as dynamic light scattering, which measures longer length scales (micrometers), or neutron spectroscopy techniques such as neutron spin echo or inelastic neutron scattering, which typically measure on faster time scales of nanoseconds and below. Clearly, experimental techniques are needed to close

[1]Department of Physics, AlbaNova University Center, Stockholm University, SE-106 91 Stockholm, Sweden. [2]Institut für Angewandte Physik, Universität Tübingen, Auf der Morgenstelle 10, 72076 Tübingen, Germany. [3]Department Physik, Universität Siegen, Walter-Flex-Strasse 3, 57072 Siegen, Germany. [4]ESRF - The European Synchrotron, 71 Avenue des Martyrs, CS 40220, 38043 Grenoble Cedex 9, France. [5]Institut Laue-Langevin, 71 Avenue des Martyrs, CS 20156, 38042 Grenoble Cedex 9, France. [6]European X-Ray Free-Electron Laser Facility, Holzkoppel 4, 22869 Schenefeld, Germany. ✉e-mail: mario.reiser@fysik.su.se; f.perakis@fysik.su.se; christian.gutt@uni-siegen.de
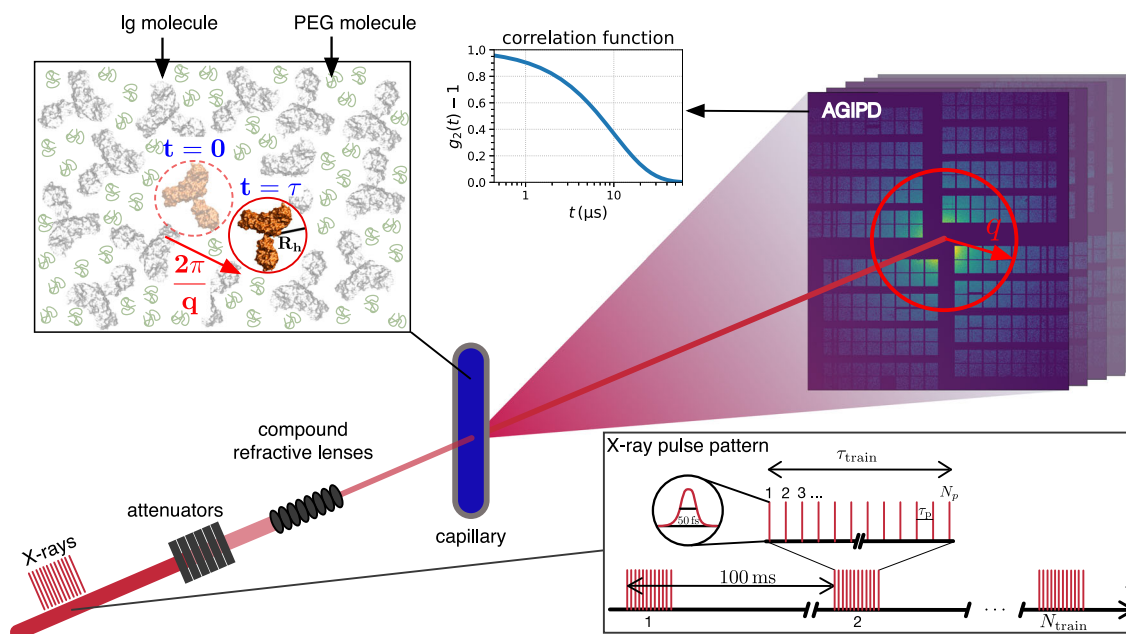
Fig. 1 | Scheme of the experiment. Highly concentrated solutions of immunoglobulin (Ig) with polyethylene glycol (PEG) are measured in quartz capillaries. An individual Ig molecule has a hydrodynamic radius of $R_h = 5.5$ nm. Megahertz X-ray photon correlation spectroscopy (MHz-XPCS) measurements are performed by using trains of X-ray pulses, which illuminate the sample. The spacing between two pulses within a train is τ_p and was varied between 443 and 886 ns where a train contains N_p individual X-ray pulses. The length of an individual X-ray pulse is ≤ 50 fs[50]. A new train is delivered every 100 ms. The train duration is determined by the number of pulses per train and the delay time between the pulses : $\tau_{train} = (N_p - 1)\tau_p$. The longest train duration during the experiment was $\tau_{train,max} = (144 - 1) \times 886$ ns ≈ 127 μs. For a period of 100 ms $- \tau_{train}$, the sample is not illuminated by X-rays. By analyzing sequential X-ray scattering patterns measured with the adaptive gain integrated pixel detector (AGIPD), information about the dynamics of the sample can be obtained in the form of intensity auto-correlation functions calculated from fluctuating speckle patterns. A measurement consists of a series of N_{train} individual trains (see Table 1).

this gap and measure collective dynamics on microsecond time scales and nanometer length scales. By analyzing fluctuating X-ray speckle patterns, MHz-XPCS is potentially capable of closing this gap, as we demonstrate here, and enables us to gain information on equilibrium and out-of-equilibrium collective dynamics of protein solutions.

Protein dynamics in crowded environments are particularly relevant in the context of intracellular transport in the cytoplasm of eukaryotic cells[10], phase transitions in biomolecular condensates[11–13], aggregation phenomena[14,15], and drug production[16]. In highly concentrated environments, the dynamics differ significantly from that of a dilute system, whereas the exact mechanisms that influence the dynamics on different time scales are not yet fully understood[6,7,17]. It was found that in vivo dynamics in cells exhibit tremendously reduced diffusion compared to in vitro measurements of diluted proteins in buffer solutions[18–25]. It is believed that the level of slowing-down depends on the particular system and possibly additional crowding agents[6,18,26–28]. In addition to excluded volume effects[29,30], there can be contributions from the local water dynamics of the hydration layer[31], quinary interactions of proteins with other cytoplasmic constituents[18,19,32–35], and transient cluster formation[36–40] that influence intracellular protein diffusion. Also, the dynamics often exhibit anomalous behavior—i.e., non-Brownian and in particular subdiffusive dynamics[26,41,42]—making it difficult to extrapolate the dynamics from the dilute regime. Clearly, new methods are needed to directly probe diffusive dynamics in crowded biological solutions on (sub-) microsecond time scales and nanometer length scales to study these phenomena.

Radiation damage constitutes a major challenge for X-ray scattering experiments with protein solutions. Radiolysis of water and the fast distribution of the free radicals formed rapidly degrade the protein molecules. Hence, a typical upper limit of tolerable absorbed doses is estimated on the order of a few kGy in these experiments with the exact value depending on the chemical composition of the system[43–46]. Protein aggregation is a signature of beam-induced damage in protein solutions visible via changes in the X-ray scattering form factor. Aggregation processes and the spread of free radicals are both driven by diffusive dynamics and act on nano- and microsecond time scales[14,47–49]. The study of such time-dependent dynamic processes in aqueous solutions of bio-molecules when illuminated with X-rays is of considerable relevance for understanding biological aspects of ionizing radiation. In addition, MHz-XFEL experiments deliver extremely high dose rates to the sample. Utilizing MHz repetition rates and high attenuation, the X-ray pulses are delivered on (sub-) microsecond time scales such that an average dose rate on the order of several kGy per microsecond can be reached. The effects of such high dose rates on structure and dynamics of protein solutions are still unknown.

Here, we report a MHz-XPCS experiment with radiation sensitive protein solutions at the Materials Imaging and Dynamics (MID) instrument[50] at EuXFEL. We investigate the dynamics in a concentrated bovine immunoglobulin (Ig) solution where 80% of the Ig is constituted by IgG[51,52]. Immunoglobulin is an abundant antibody protein that can be found, for instance, in the blood of animals and humans. Polyethylene glycol (PEG) is added to the solution as a depletant and induces attractive protein-protein interactions that—depending on concentration and temperature—can result in liquid–liquid phase separation (LLPS)[51,52]. This combination renders the Ig-PEG system an interesting candidate for the MHz-XPCS measurements in the context of both crowding dynamics in concentrated protein solutions and the formation of biomolecular condensates.

Results

Measurement scheme and data collection
We employed X-ray pulses with 443 and 886 ns delays between successive pulses corresponding roughly to repetition rates of 2.26 and 1.13 MHz, respectively. The X-ray pulses were delivered in trains of up to 200 pulses with a train frequency of 10 Hz (see Fig. 1). This time

structure makes it possible to conduct MHz-XPCS measurements within a single train, while the time between subsequent trains is sufficiently long to refresh the sample via translation.
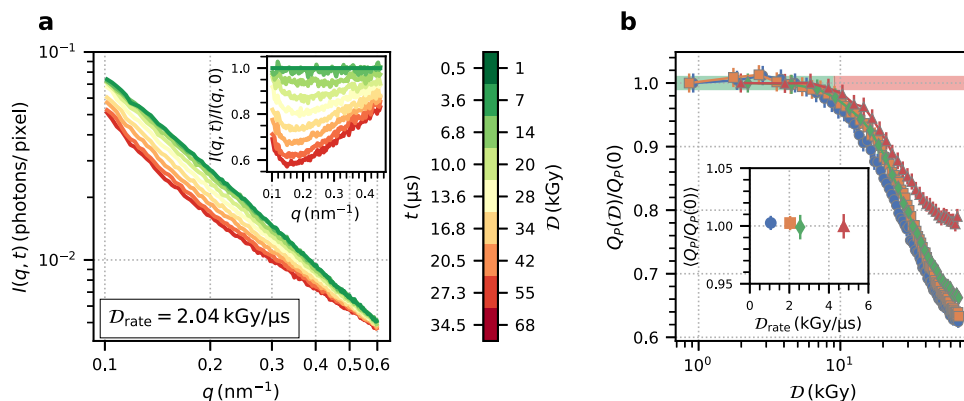
The data presented here were acquired at the MID instrument in small-angle X-ray scattering (SAXS) geometry with a pink beam, i.e., using self-amplified spontaneous emission (SASE) without a monochromator, and a photon energy of 9 keV[50]. A sketch of the experimental setup is shown in Fig. 1. The Adaptive Gain Integrating Pixel Detector (AGIPD)[53] was placed 7.46 m behind the sample with most of the sample-detector flight path being evacuated. The Ig-PEG solutions were filled into quartz capillaries with an outer diameter of 1.5 mm and a wall thickness of 20 μm. A Linkam scientific instruments stage was used to control and stabilize the sample temperature at 298 K, which is above the binodal in the single phase regime of the Ig-PEG system[51,52]. The X-ray beam was focused to a diameter of 10 μm (FWHM) using compound refractive lenses to increase the measured speckle contrast and the signal-to-noise ratio (SNR) of the XPCS measurements[54].

Table 1 contains a summary of the measurement parameters. The intensity of the X-rays was reduced by chemically vapor deposited (CVD) diamond attenuators of various thickness and adjusted such that the samples were exposed to the lowest possible dose while keeping the scattered intensity high enough to reach a sufficient SNR. For example, with an average pulse energy of 1.2 mJ and 3925 μm CVD attenuator thickness 6.5×10^8 photons per X-ray pulse illuminate the sample. The incoming flux results in an average scattering signal of less than 10^{-1} photons per pixel per image. In addition to the absolute dose also the average dose rate was varied, i.e., the absorbed dose per time, measured in kGy μs^{-1}. The actual dose rate value is calculated as an average over the first ten X-ray pulses and all trains of a measurement (see "Methods").

Table 1 | Measurement parameters

$\mathcal{D}_{rate}$ (kGy μs^{-1})	f_{FEL} (MHz)	τ_p (ns)	T_{cvd} (%)	$\langle \Phi_c \rangle$ (10^8ph/pls)	N_{train}	N_p
1.06	1.13	886	0.6	1.59	2800	144
2.04	2.26	443	0.6	1.53	9200	200
2.55	1.13	886	1.4	3.82	2000	144
4.75	2.26	443	1.4	3.56	5200	200

$\mathcal{D}_{rate}$ is the average dose rate, f_{FEL} is the XFEL frequency, and τ_p is the time between successive pulses which defines the the minimum XPCS delay time. T_{cvd} is the transmission of the diamond attenuators which results in the average number of incident photons per X-ray pulse (ph/pls) on the sample, $\langle \Phi_c \rangle$. N_{train} is the number of pulse trains averaged in the analysis. N_p is the maximum number of pulses per train.

## Megahertz small-angle X-ray scattering (MHz-SAXS)

The evolution of the time-resolved SAXS signal as a function of dose and dose rate is analyzed by computing the azimuthally integrated intensity $I(q, t)$ as a function of absolute momentum transfer, $q = 4\pi/\lambda \sin(2\theta/2)$, where λ is the X-ray wavelength and 2θ is the scattering angle, and measurement time or dose (see Fig. 2a). The absorbed dose is proportional to the measurement time and is calculated with Eq. (5) (see "Methods"). The data displayed were recorded with a dose rate of 2.04 kGy μs^{-1}, but with absolute doses varying between 1 kGy (green) and 74 kGy (red). With increasing dose, we observe significant changes in $I(q, t)$, with the largest decrease of intensity visible at momentum transfers of $q = 0.17$ nm^{-1} accompanied by an increasing scattering signal at small momentum transfers. The inset shows the data normalized by $I(q, 0)$. The Ig-PEG system exhibits a structure factor peak close to 0.62 nm^{-1} that was studied in a previous work by Da Vela et al.[51]. Additionally, the phase behavior of the Ig-PEG systems is characterized by an upper critical solution temperature of around 294 K. The overall decrease of intensity in Fig. 2 indicates that the system is moving away from the LLPS binodal in the phase diagram, presumably due to beam-induced local heating. Deeper in the single phase regime, increasingly repulsive protein-protein interactions lead to a reduced SAXS intensity. On the other hand, at q-values below 0.17 nm^{-1}, the visible increase of $I(q, t)/I(q, 0)$ indicates the formation of X-ray induced aggregation of the proteins.

We quantify the evolution of structural changes by calculating the Porod invariant

$$Q_P(t) = \int_{q_{min}}^{q_{max}} q^2 I(q, t)\, dq, \qquad (1)$$

in the accessible q-range ($q_{min} = 0.1$ nm^{-1}, $q_{max} = 0.6$ nm^{-1}) as a function of dose (see Fig. 2b). $Q_P(\mathcal{D})$ displays an initial plateau up to a maximum dose of 10 kGy after which it starts to decrease more than two percent from its initial value. At doses below 10 kGy, the protein structure seems unaffected by the X-ray illumination—at least on the length scales probed here. In this low-dose regime, we also extract the dose rate dependence of the Porod invariant by averaging the $Q_p(\mathcal{D})$ data for $\mathcal{D} < 10$ kGy. The results are displayed in the inset in Fig. 2b demonstrating the absence of a dose rate dependence in the SAXS signal. This is in agreement with previous work reporting that the absolute absorbed dose is the main driver for radiation damage and dose rate effects are only weak[46].

Fig. 2 | Static scattering signal of Ig-PEG. a The azimuthally integrated intensity, $I(q, t)$, as a function of momentum transfer, q. The color indicates the absorbed dose $\mathcal{D}$ and the corresponding timescales. The data shown are acquired with a dose rate of 2.04 kGy μs^{-1}. The inset displays $I(q, t)$ normalized to the first pulse $I(q, 0)$. **b** Porod invariant, $Q_P(\mathcal{D})$, calculated from the data displayed in **a** (orange) and three additional dose rates. The data are normalized to $Q_P(0)$ and the error bars are calculated as the standard deviation of the normalized second pulse from unity. The inset shows the mean of $Q_P(\mathcal{D})$ below 10 kGy for different dose rates. The error bars indicate the weighted standard deviation of Q_P in this range. Source data are provided as a Source Data file.
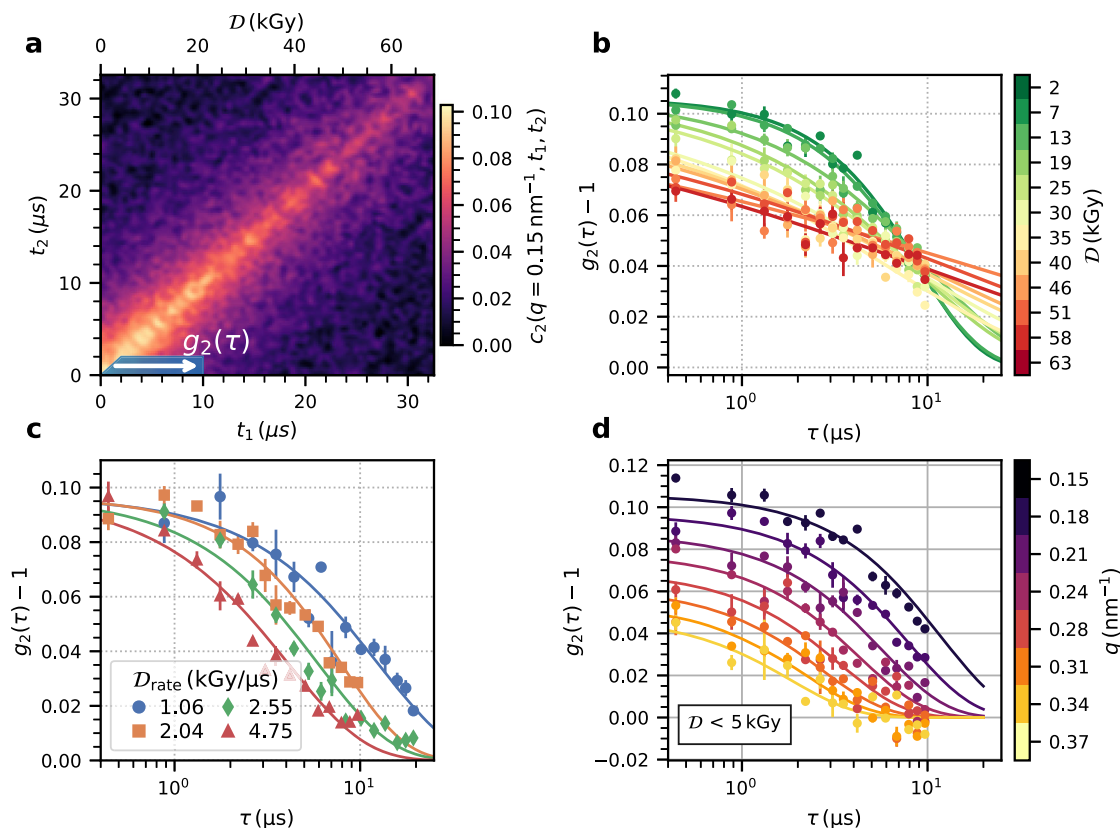
Fig. 3 | Correlation functions. a Two-time correlation function, c_2, of Ig-PEG measured with an average dose rate of 2.04 kGy μs⁻¹ for $q = 0.15$ nm⁻¹. **b** Correlation functions for different initial doses ($\mathcal{D}_{rate} = 2.04$ kGy μs⁻¹, $q = 0.15$ nm⁻¹). **c** Correlation functions with an initial dose below 5 kGy for different dose rates

at $q = 0.15$ nm⁻¹. **d** Correlation functions for different momentum transfers fitted with a q-squared dependent relaxation rate ($\mathcal{D}_{rate} = 2.04$ kGy μs⁻¹). The error bars represent the standard error over pixels and repetitions. Source data are provided as a Source Data file.

Megahertz X-ray photon correlation spectroscopy (MHz-XPCS)
The disordered protein solutions give rise to a speckle pattern in the far-field when illuminated by coherent radiation. The dynamics can be studied by analyzing the speckle intensity fluctuations that are related to the microscopic motion of the protein molecules. The intensity $I_p(q,t)$ is measured at time t by pixel p within a concentric region of interest (ROI) of constant absolute momentum transfer. We utilized an XPCS adapted acquisition scheme in which the sample is continuously moving through the X-ray beam with a velocity of 400 μm s⁻¹. The sample movement is negligible during an X-ray train ensuring illumination of the same sample spot on microsecond time scales. In between two trains the sample position offset is large enough to completely renew the sample volume, and thus to avoid accumulated damage. The low intensity scattering signal requires averaging correlation functions from many trains (between 2000 and 9000 see Table 1) to increase the SNR. Approximately 80% of the acquired trains are used for the XPCS analysis while the rest are discarded after applying filters based on diagnostics such as extremely low intensity due to the SASE fluctuations.

We compare measurements with average dose rates, $\mathcal{D}_{rate}$, from 1.06 to 4.75 kGy μs⁻¹. The influence of dose and dose rate on the protein dynamics can be quantified with the help of two-time correlation functions (TTCs)[55,56] which essentially represent the correlation coefficient between speckle images taken at times t_1 and t_2 at momentum transfer q:

$$c_2(q,t_1,t_2) = \left\langle \frac{\langle I_p(q,t_1) I_p(q,t_2) \rangle_p}{\langle I_p(q,t_1) \rangle_p \langle I_p(q,t_2) \rangle_p} \right\rangle_j - 1. \quad (2)$$

Here, $\langle ... \rangle_p$ denotes an average over all pixels with the same absolute momentum transfer, q, and $\langle ... \rangle_j$ denotes an average over all trains where $j = 1...N_{train}$. The data calibration and analysis workflow for MHz-XPCS with AGIPD is described in detail in Dallari et al.[3].

Figure 3a displays a TTC measured with an average dose rate of 2.04 kGy μs⁻¹ at $q = 0.15$ nm⁻¹. The abscissa and ordinate of the TTC show the measurement times t_1 and t_2, respectively, within an X-ray pulse train while the additional label at the top indicates the corresponding absorbed dose. The TTC decays with increasing distance from the diagonal describing the temporal decorrelation of the speckle fluctuations due to the sample dynamics. The fact that the diagonal does not exhibit a constant width indicates that the dynamics change throughout the measurement.

Time-resolved intra-train intensity auto-correlation functions, $g_2(q,\tau,\mathcal{D}(t_0))$, are calculated by averaging sections of the TTCs as indicated by the white arrow in Fig. 3a:

$$g_2(q,\tau,\mathcal{D}(t_0)) = \langle c_2(q,t_1 = t_0 \pm \Delta t + \tau, t_2 = t_0 \pm \Delta t) \rangle_{\Delta t} + 1. \quad (3)$$

To obtain the correlation function for a particular initial dose, $\mathcal{D}(t_0)$, during the measurement, the time t_0 is chosen on the diagonal of the TTC in Fig. 3a, while noting that the dose increases further with each point of the correlation function. The average over Δt can be seen as rebinning c_2 along t_2 to increase the statistics. This approach yields a set of $g_2(q,\tau)$ per dose and dose rate.

The correlation functions are modeled by a Kohlrausch–Williams–Watts (KWW) function:

$$g_2(q,\tau) = 1 + \beta(q)\, e^{-2(\Gamma(q)\tau)^\alpha}, \quad (4)$$
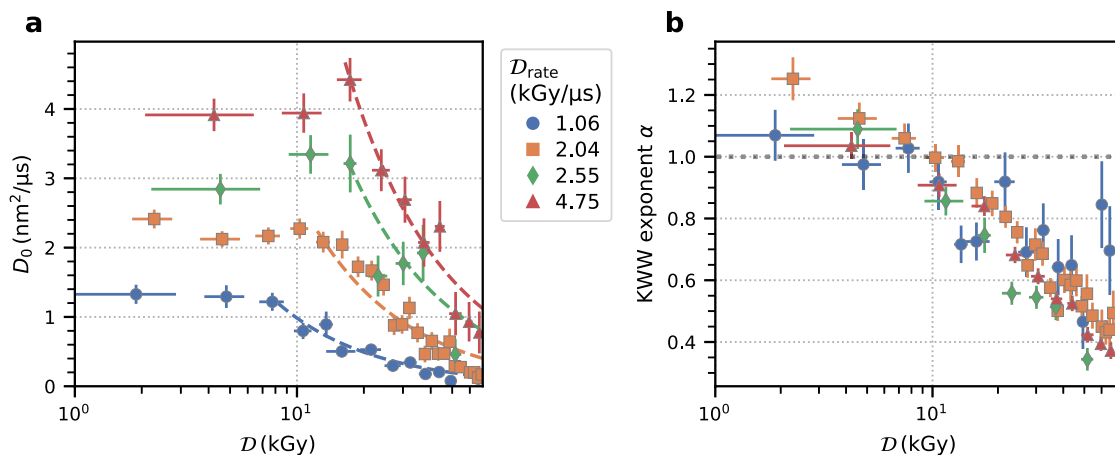
Fig. 4 | Dynamical parameters. a Diffusion coefficient, D_0, as a function of initial dose for different dose rates indicated by the color. The dashed lines are guides to the eye. **b** KWW exponent for different dose rates as a function of total absorbed dose. Source data are provided as a Source Data file.

where $\beta(q)$ is the q-dependent speckle contrast[57] ($\beta(q = 0.15\ nm^{-1}) \approx 11\%$) and α is the KWW exponent. Brownian diffusion is characterized by a quadratic q-dependence of the relaxation rates $\Gamma(q) = D_0 q^2$, where D_0 is the diffusion coefficient, and simple exponential behavior ($\alpha = 1$). KWW exponents smaller than 1 are typically observed in supercooled liquids and gels and can indicate heterogeneous dynamics with a distribution of relaxation times[58]. A quadratic q-dependence and a q-independent KWW exponent are used to model the data. Figure 3d shows that within the experimental accuracy the KWW function describes the data well.

Figure 3c shows correlation functions for different dose rates for absolute doses below 5 kGy. The data indicates that the dynamics become faster with dose rate as the correlation functions shift to shorter time scales while the overall lineshape appears to change only slightly. This is different from the behavior observed with increasing total dose in Fig. 3b where the shape of the correlation functions drastically changes from a simple exponential decay at low doses to a highly stretched ($\alpha < 1$) and almost logarithmic decay at higher dose values. We account for these changing KWW exponents by computing the average relaxation rate[59,60] $\langle\Gamma\rangle(q) = \Gamma(q)\alpha/\Gamma_f(1/\alpha)$, where $\Gamma_f(x)$ is the Γ-function. Using these average relaxation rates one pair of parameters (D_0, α) is calculated per initial dose and dose rate, where $D_0 = \langle\Gamma\rangle(q)/q^2$. The results are displayed in Fig. 4. The diffusion coefficients in Fig. 4a reveal a pronounced dependence on the initial dose and dose rate as already indicated by the correlation functions in Fig. 3 and are higher than expected for the base temperature of $T_0 = 298$ K. Therefore, we denote D_0 reported here is as an effective diffusion coefficient discussed in more detail in the following section. The numbers obtained for D_0 are on the order of a few $nm^2\ \mu s^{-1}$, which is the typical range of diffusion coefficients found for dense protein systems[6,7,26]. For a given dose rate, all diffusion coefficients follow a similar pattern as a function of initially absorbed dose: D_0 is nearly independent of the initial dose up to a threshold value, above which the D_0 steadily decreases. The threshold initial dose is slightly below 10 kGy for a dose rate of 1.06 kGy μs^{-1} and increases above 15 kGy for 4.75 kGy μs^{-1}. The average values of D_0 below these thresholds increase linearly by about a factor of four from 1.3 to 4 $nm^2\ \mu s^{-1}$ with increasing dose rate. The corresponding KWW exponents do not show any pronounced dose rate dependence, but a clear dependence on the initial dose (Fig. 4b). The KWW exponents further reveal that the correlation functions exhibit a simple exponential shape ($\alpha = 1$) for low doses, while they are increasingly stretched above 10 kGy, which approximately coincides with the dose value where a decrease in D_0 becomes apparent (Fig. 4a). The simultaneous decrease of D_0 and the KWW exponent for high doses points towards beam-induced aggregation of the proteins (cf. Fig. 2), which results in slower diffusion and increasingly stretched exponential behavior.

Discussion

Our results indicate that static and dynamic properties are influenced in different ways by the intense X-ray pulses of the European XFEL. MHz-SAXS reveals that the static scattering signal—within the accessible q-window—is preserved below an absorbed dose of 10 kGy. This threshold value is independent of the applied dose rate (Fig. 2b inset) within the limited range of dose rates. It is noteworthy that the extremely high dose rates and microsecond time scales probed with an XFEL yield similar threshold values ($\approx$10 kGy) as the orders of magnitude lower dose rates used at a synchrotron ($\approx$1 kGy s^{-1} [52]).

Understanding the dose rate dependence of radiation-induced effects is crucial for comparing and optimizing experiments at different radiation sources (rotating anodes, synchrotrons, XFELs). At comparably moderate dose rates of tens of Gray per second at synchrotrons, the aggregation rate of proteins was found to exhibit a dose rate dependence[46] favoring measurements with low dose rates. On the other hand, high dose rates seem to be preferable in room temperature protein crystallography measurements[61–63].

Generally, radiation damage in aqueous protein solutions is mainly attributed to the diffusion and successive reaction of proteins with radicals produced by radiolysis, such as OH$^-$. Radiolysis itself involves a variety of different time and length scales where the radicals are not uniformly generated in the solvent, but distributed initially in nanoscale traces which broaden and diffuse into the bulk on timescales of hundreds of nanoseconds to microseconds during the chemical stage[64]. The primary yield of OH$^-$ radicals is high, with 2.87 OH$^-$ per 100 eV absorbed after one microsecond[65], leading to an average of about 0.6 OH$^-$ radicals per Ig protein molecule needed to induce measurable changes to the SAXS signal (see Fig. 2). The observed threshold dose of 10 kGy represents a typical time window of 9.4 μs when using a dose rate of 1.06 kGy μs^{-1}. The absence of a measurable dose rate effect on this static threshold value indicates that diffusion rates of radicals, recombination, and quenching effects do not affect the overall agglomeration probability.

Additional insight can be obtained from the MHz-XPCS data, which allows to trace time-resolved non-equilibrium dynamics via the TTCs. With regard to protein diffusion the typical mean square distances probed here can be estimated via

$$g_2(q,\tau) - 1 = \beta \exp(-q^2 \langle \Delta x^2(\tau) \rangle / 6)$$
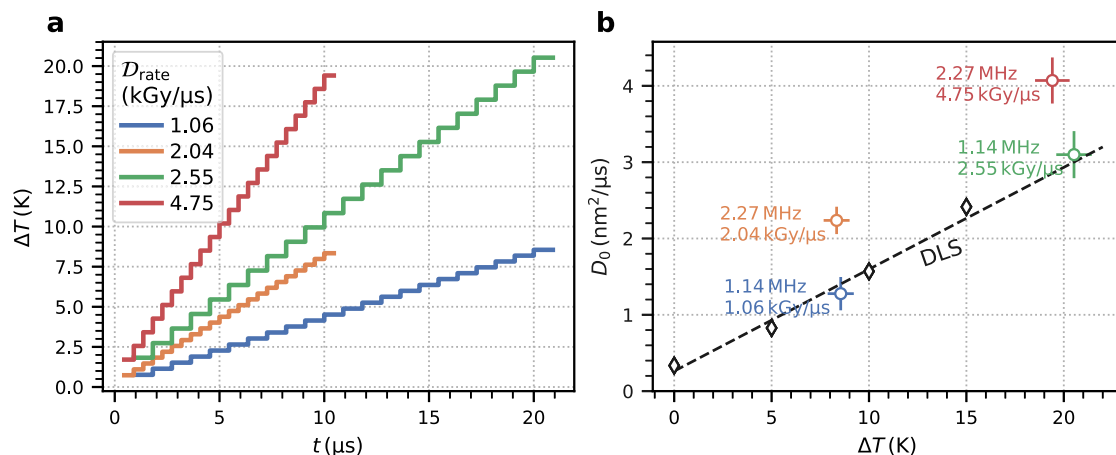
Fig. 5 | Effect of temperature on the dynamics. a Calculated temperature increase ΔT after 20 XFEL pulses for the four different dose rates. **b** Diamonds: Temperature dependence of diffusion coefficients measured by dynamic light scattering (DLS). The dashed black line is a linear fit to the data. Circles: diffusion constants determined via XPCS and minimum initial dose using the pulse frequency and dose rate indicated. The temperature assigned to the XPCS diffusion constants is estimated based on the respective temperature rise shown in **a**. The base temperature was $T_0 = 298$ K for all XPCS measurements. Source data are provided as a Source Data file.

yielding values of $\sqrt{\langle \Delta x^2 \rangle} = 16$ nm at $q = 0.15$ nm^{-1} to $\sqrt{\langle \Delta x^2 \rangle} = 4$ nm at $q = 0.6$ nm^{-1} at $1/e$ decay of the correlation functions. Thus, in the present configuration, MHz-XPCS is sensitive to the motion inside the first coordination shell of the protein molecules in the dense solution.

Furthermore, it is interesting to examine the dynamics at dose values below the static damage threshold of 10 kGy obtained from the MHz-SAXS analysis. The diffusion constants are almost independent of the initial dose for a given dose rate. However, D_0 displays a pronounced rate dependence and increases by almost a factor of four between the lowest and the highest dose rate (Fig. 4b). Illuminating a sample with highly intense X-ray pulses can lead to a temperature increase. Based on the X-ray beam size of 10 μm, we estimate that the generated heat dissipates with a time constant of 310 μs (see "Methods" section below), which is much longer than the measurement window covered by a g_2-function here (20 μs). Thus, the illuminated sample volume does not cool down noticeably during a measurement and the maximum accumulated heat only depends on the fluence per pulse and the number of pulses illuminating the same sample volume which is equivalent to the accumulated dose.

The increase of temperature for the different XFEL parameters is estimated following the model used by Lehmkühler et al.[1] using a weighted average heat capacity of the constituents of $c_p = 3.42$ J g^{-1} K^{-1}. With a maximum number of 3.82×10^8 photons per X-ray pulse (see Table 1) the energy density is 5.5 mJ mm^{-2}, which is an order of magnitude smaller than in the work of Lehmkühler et al.[1]. Fig. 5a displays the corresponding temperature rise during a pulse train with a temperature increase of $\Delta T \approx 8$ K after the low intensity pulse trains (blue and orange) and $\Delta T \approx 19$–21 K after the high intensity pulse trains (red and green). For comparison, we measured the temperature dependence of the equilibrium diffusion constant with dynamic light scattering (DLS), where the sample was equilibrated at each temperature before a measurement, and display the results in Fig. 5b. The values of D_0 measured with MHz-XPCS and X-ray pulse repetition rates of 1.13 MHz are close to their equilibrium values obtained from DLS, when taking the XFEL-induced temperature increase into account. In contrast, employing higher XFEL frequencies of 2.26 MHz yields consistently higher diffusion coefficients which cannot be explained by a temperature increase alone. We hypothesize that the intense MHz XFEL pulses create a non-equilibrium state triggering processes on the sub-microsecond time scale. One example of such processes is the spatial homogenization of the aforementioned radiolysis products. The typical rates of secondary products such as OH$^-$ radicals are on the order of microseconds[66,67]. Thus, on sub-microsecond time scales, the XFEL pulses simultaneously produce and probe a spatially inhomogeneous local distribution of the radiolysis products. The resulting chemical gradients, molecular repulsion due to dose rate-dependent protein charging, and possibly changes of the ionic strength of the solution, as well as damage to the PEG molecules, could contribute to the observed enhanced diffusive motion. Clearly, more systematic data and additional work by theory and simulation is needed to understand this XFEL-driven motion.

The question arises why the faster dynamics at higher dose rates do not lead to a dose rate-dependent aggregation visible in the SAXS signal. We address this question by employing the Stokes–Einstein relation and estimating the temporal evolution of the relative changes to the apparent hydrodynamic radii via $R_h(t)/R_h(0) = D_0(0)/D_0(t)$, where $D_0(0)$ and $R_h(0)$ represent the respective values at the minimum dose in Fig. 4. The increase of this ratio serves as an indicator for protein aggregation. Figure 6 shows that aggregation sets in earlier and develops faster for higher dose rates. For a dose rate of 1.06 kGy μs^{-1}, $R_h(t)/R_h(0)$ has approximately doubled after (18.0 ± 0.9) μs and after (6.8 ± 0.6) μs for 4.75 kGy μs^{-1} (see Supplementary Fig. 4). Using the measured diffusion coefficients D_0, we further calculate the time-dependent root mean square displacement (RMSD) $\sqrt{\langle \Delta x^2(t) \rangle} = \sqrt{6 D_0 t}$ of the proteins and plot $R_h(t)/R_h(0)$ as a function of RMSD (see Fig. 6b). The data for the different dose rates collapse onto a single master curve (red line) indicating that the onset of aggregation mainly depends on the RMSD of the protein molecules. Higher dose rates induce faster movement of the proteins, and thus the RMSD necessary for aggregation is reached earlier. Figure 6b also reveals that aggregation sets in after a RMSD of about 10 nm and the space a single protein can explore in the crowded solution before that happens is indicated by a red dashed circle. This area is quite large considering that the sample is a densely packed solution of 250 mg ml^{-1}, where the mean free path l between two molecules is typically smaller than their radius. We estimate $l = 1/(n\pi(2R_h)^2) = 2.6$ nm from the number density n and the molecular radius $R_h = 5.5$ nm of an Ig molecule which in turn implies an average number of contacts between proteins on the order of $N = \langle \Delta x^2(t) \rangle / l^2 \approx 14$ before aggregation sets in.

Our analysis indicates that aggregation is not strictly translational diffusion limited, but multiple contacts are necessary to attach two protein molecules to each other and form aggregates. This may hint towards the importance of specific interaction sites driving the
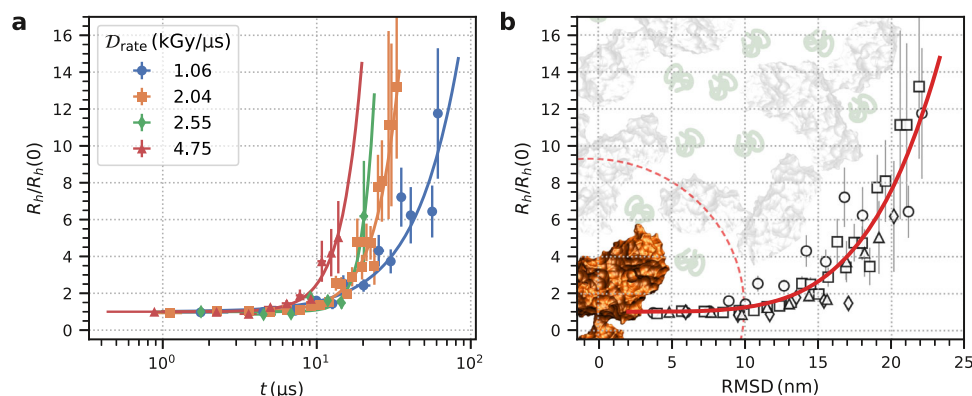
Fig. 6 | X-ray induced aggregation pathways. a Apparent hydrodynamic radii normalized to the initial value $R_h(0)$ as a function of measurement time for different dose rates. The solid lines are guides to the eye. **b** Apparent hydrodynamic radii normalized to the initial value $R_h(0)$ as a function of root mean square displacement (RMSD). The red solid line is a guide to the eye. The dashed red circle describes a sphere with a radius of about 10 nm and marks the space an Ig molecule can explore before the onset of aggregation. Source data are provided as a Source Data file.

aggregation process[68]. In addition, we note that unfolding processes, which increase the protein propensity to aggregate do also occur on time scales of microseconds[69]. Thus, the observed initial period of constant R_h points towards a minimum incubation time on the order of 10 μs before the proteins locally unfold or a time needed for rotational motion of molecules in order to allow activated sites to form local bonds. This incubation time and the minimum RMSD of 10 nm define a window of opportunity where dynamics can be measured in a *correlation before aggregation* scheme. Analogously to *diffraction before destruction* on femtosecond time scales[70–73], *correlation before aggregation* will allow to obtain experimental information about the structural sample dynamics on (sub-)microsecond time scales before X-ray induced changes will become apparent in the XPCS signal. Additional data with more dose rates could allow developing novel methods to estimate the diffusion coefficients at zero dose rate[74]. However, the dose rate dependence might be highly dependent on the sample. On the other hand, developing the *correlation before aggregation* approach further would provide a window of opportunity, where with moderate doses and dose rates, the SNR is increased and the overall measurement time and sample consumption could be reduced.

Reducing the sample consumption is crucial for measuring particularly precious solutions or systems that exhibit phase transitions on microsecond time scales, e.g., biomolecular condensates, which is hard to repeat thousands of times[52,58,75]. Improving the experiments could be achieved for instance by making use of the self-seeding schemes which provide a much larger longitudinal coherence length. A larger longitudinal coherence length would allow for a larger beam size with similar measured speckle contrast yielding a lower photon density on the sample. This reduces the radiation damage to the sample and the amount of sample needed. It also increases the scattering volume and scattering intensity and thus strongly increases the SNR ratio[76]. Further technical improvements such as MHz detectors with smaller pixel size are needed to improve the SNR even further which allows extending the accessible q-range and lowering the dose rate needed.

Summarizing, we demonstrated that MHz-XPCS bears the potential to become a useful tool for measuring dynamics of biological macromolecules in solution on molecular length scales and on the time scales relevant for diffusive motion in cells. Importantly, our results indicate that taking the temperature rise of the solution into account allows for studying equilibrium dynamics within the first coordination shell of the molecules. Higher XFEL frequencies drive the dynamics and lead to increasing diffusion coefficients and aggregation which sets in after a time window of 10 μs. We refer to

this approach as correlation before aggregation which allows to capture protein dynamics in solution before the manifestation of X-ray-induced effects. Additional experiments and simulations are needed to fully understand the underlying physics of the involved processes. Understanding the observed dose rate dependence of the diffusion process involves accurate knowledge of a number of yet unknown factors, such as the role of the interaction potentials, concentration, solvent chemical composition, and size and masses of the proteins. Resolving these properties and the role of radiolysis processes and their products in this context will determine the best data acquisition strategies for measuring the unperturbed dynamic properties.

Methods

Sample preparation
The sample preparation followed a procedure provided by the literature[51]. Polyclonal bovine immunoglobulin (purity ≥99%, Sigma-Aldrich, SRE0011), PEG 1000 (Sigma-Aldrich, 81188), NaCl (Merck 106404), HEPES (Roth, HN78), and NaN$_3$ (Sigma-Aldrich, S8032) were used as received. All solutions were prepared in a buffer of composition 20 mM HEPES pH = 7.0, 2 mM NaN$_3$, using degassed Milli-Q water (Merck Millipore 18.2 MΩ cm). The concentration of the immunoglobulin stock solution was assessed by UV absorption at 280 nm, using an extinction coefficient of $e_{280} = 1.4$ mL mg^{-1} cm^{-1} with a Cary 50 UV–Vis spectrophotometer. The experimental phase diagram of this system has been established in our previous work[51]. The "parent solution" was equilibrated for about 24 h at 294 K and then briefly centrifuged, resulting in a clear dense and a dilute phase, separated by a sharp meniscus. The parent solution composition was immunoglobulin 200 mg/mL, PEG 12% w/v and NaCl 150 mM. The dense liquid phase was used for XPCS measurements with a concentration of roughly 250 mg mL^{-1}.

Measurement protocol
The sample was moved continuously through the X-ray beam to refresh the sample volume between trains. The translation motor speed was 0.4 mm s^{-1} leading to an absolute sample translation of 40 μm between successive trains (a train arrives every 100 ms). X-ray generated heat diffuses with a thermal diffusion constant of $D_T = 0.143$ mm^2 s^{-1}. Assuming homogeneous heat diffusion in radial direction perpendicular from the beam, after $\tau_{train} = 100$ ms the heat diffused in a cylinder with radius $\sqrt{6 D_T \tau_{train}} \approx 293$ μm. The illuminated volume of the next train is then 10 μm^2/293 μm^2 ≈ 0.1% of that volume. Therefore, beam-induced heating effects generated by the previous train can be neglected for the following illumination.

Calculation of the absorbed dose and dose rate

On the time scale of an individual X-ray pulse ($\leq 50\,\mathrm{fs}$[50]) and with maximum flux, the peak dose rate can reach several hundred MGy per pulse[77]. Utilizing MHz repetition rates and high attenuation, the X-ray pulses are delivered on (sub-) microsecond time scales such that an average dose rate on the order of several kGy per microsecond can be reached. Correspondingly, synchrotron sources produce typical average dose rates of kGy per second.

In order to quantify the amount of energy absorbed by a certain sample mass, we calculate the dose, $\mathcal{D}(N_p)$, absorbed by the sample after N_p pulses:

$$\mathcal{D}(N_p) = \left\langle \sum_{i=1}^{N_p} \frac{\Phi_c^j(i) E_c A}{z^2 d_s \rho} \right\rangle_j, \qquad (5)$$

where $A = (1 - e^{-d_s/\mu_{\mathrm{eff}}})$ denotes the sample absorption where $d_s = 1.5$ mm is the sample thickness and $\mu_{\mathrm{eff}} = 1.35$ mm is the effective attenuation length of the solution calculated as the weighted harmonic mean of the individual components[52,78], $E_c = 9$ keV the photon energy, $\Phi_c^j(i)$ the number of photons in pulse i in train j, $\rho = 1.09\,\mathrm{g\,cm^{-3}}$ is the sample density, and $z = 10\,\mu\mathrm{m}$ is the beam size. $\langle\ldots\rangle_j$ denotes an average over trains. The dose is measured in Gray (1 Gy = 1 J kg^{-1}).

To account for SASE related intensity fluctuations, the average dose rate is calculated as the average dose absorbed by the sample after ten pulses divided by the delay between two successive pulses, τ_p:

$$\mathcal{D}_{\mathrm{rate}} = \frac{\mathcal{D}(N_p = 10)}{10\tau_p}. \qquad (6)$$

Error bar calculation

The error bars of the correlation functions in Fig. 3 are calculated as the standard deviation of the fluctuations of the contrast values within a q-bin. This standard deviation is used to calculate the weighted average over trains and times in Eqs. (2) and (3). These error bars are used in the fits for the estimation of the parameters. The error bars in the following plots, which display the fit results of the correlation functions, indicate the parameter uncertainty obtained from the fits using least-squares minimization.

X-ray induced heating

The relaxation time of heat diffusion used in Fig. 5 to estimate the X-ray induced heating is calculated as $\tau_{\mathrm{heat}} = c_p \rho z^2 / (2k_w) = 310\,\mu\mathrm{s}$, where $c_p = 3.42\,\mathrm{J\,g^{-1}\,K^{-1}}$ is the heat capacity of the solution and $k_w = 0.6\,\mathrm{W\,m^{-1}\,K^{-1}}$ is the thermal conductivity. The heat capacity is calculated by an average of the heat capacities of water, PEG, and IgG weighted with their volume fractions. The temperature increase induced by a pulse with energy E_p is $\Delta T_{\max} = 4\log(2)E_p/(2\pi c_p \rho z^2 \mu_{\mathrm{eff}})$. This formalism leads to values from $\Delta T = 0-21$ K depending on E_p and the number of X-ray pulses (see Fig. 5). It should be noted that 1% and less of the maximum possible E_p at MID has been used to reduce beam-induced effects.

Reporting summary

Further information on research design is available in the Nature Research Reporting Summary linked to this article.

Data availability

The data are available from the authors upon request. Source data are provided with this paper.

Code availability

Analysis scripts are available from the authors upon request.

References

1. Lehmkühler, F. et al. Emergence of anomalous dynamics in soft matter probed at the European XFEL. *Proc. Natl. Acad. Sci. USA* **117**, 24110–24116 (2020).
2. Dallari, F. et al. Microsecond hydrodynamic interactions in dense colloidal dispersions probed at the European XFEL. *IUCrJ* **8**, 775–783 (2021).
3. Dallari, F. et al. Analysis strategies for MHz XPCS at the European XFEL. *Appl. Sci.* **11**, 8037 (2021).
4. García de la Torre, J., Huertas, M. L. & Carrasco, B. Calculation of hydrodynamic properties of globular proteins from their atomic-level structure. *Biophys. J.* **78**, 719–730 (2000).
5. Ridgway, D. et al. Coarse-grained molecular simulation of diffusion and reaction kinetics in a crowded virtual cytoplasm. *Biophys. J.* **94**, 3748–3759 (2008).
6. Grimaldo, M., Roosen-Runge, F., Zhang, F., Schreiber, F. & Seydel, T. Dynamics of proteins in solution. *Q. Rev. Biophys.* **52**, E7 (2019).
7. Roosen-Runge, F. et al. Protein self-diffusion in crowded solutions. *Proc. Natl. Acad. Sci. USA* **108**, 11815–11820 (2011).
8. Von Bülow, S., Siggel, M., Linke, M. & Hummer, G. Dynamic cluster formation determines viscosity and diffusion in dense protein solutions. *Proc. Natl. Acad. Sci. USA* **116**, 9843–9852 (2019).
9. Grimaldo, M. et al. Protein short-time diffusion in a naturally crowded environment. *J. Phys. Chem. Lett.* **10**, 1709–1715 (2019).
10. Leeman, M., Choi, J., Hansson, S., Storm, M. U. & Nilsson, L. Proteins and antibodies in serum, plasma, and whole blood-size characterization using asymmetrical flow field-flow fractionation (AF4). *Anal. Bioanal. Chem.* **410**, 4867–4873 (2018).
11. Myung, J. S. et al. Weak shape anisotropy leads to a nonmonotonic contribution to crowding, impacting protein dynamics under physiologically relevant conditions. *J. Phys. Chem. B* **122**, 12396–12402 (2018).
12. Bucciarelli, S. et al. Dramatic influence of patchy attractions on short-time protein diffusion under crowded conditions. *Sci. Adv.* **2**, e1601432 (2016).
13. Tang, L. Protein translation inside synthetic membraneless organelles. *Nat. Methods* **16**, 456–456 (2019).
14. Pease, L. F., Elliott, J. T., Tsai, D.-H., Zachariah, M. R. & Tarlov, M. J. Determination of protein aggregation with differential mobility analysis: Application to IgG antibody. *Biotechnol. Bioeng.* **101**, 1214–1222 (2008).
15. Martin, N. et al. Prevention of thermally induced aggregation of IgG antibodies by noncovalent interaction with Poly(acrylate) derivatives. *Biomacromolecules* **15**, 2952–2962 (2014).
16. Skar-Gislinge, N. et al. A colloid approach to self-assembling antibodies. *Mol. Pharm.* **16**, 2394–2404 (2019).
17. Girelli, A. et al. Molecular flexibility of antibodies preserved even in the dense phase after macroscopic phase separation. *Mol. Pharm.* **18**, 4162–4169 (2021).
18. Wang, Y., Li, C. & Pielak, G. J. Effects of proteins on protein diffusion. *J. Am. Chem. Soc.* **132**, 9392–9397 (2010).
19. Li, C., Wang, Y. & Pielak, G. J. Translational and rotational diffusion of a small globular protein under crowded conditions. *J. Phys. Chem. B* **113**, 13390–13392 (2009).
20. London, R., Gregg, C. & Matwiyoff, N. Nuclear magnetic resonance of rotational mobility of mouse hemoglobin labeled with (2-13C) histidine. *Science* **188**, 266–268 (1975).
21. Williams, S., Haggie, P. & Brindle, K. 19F NMR measurements of the rotational mobility of proteins in vivo. *Biophys. J.* **72**, 490–498 (1997).
22. Ando, T. & Skolnick, J. Crowding and hydrodynamic interactions likely dominate in vivo macromolecular motion. *Proc. Natl. Acad. Sci. USA* **107**, 18457–18462 (2010).

23. Wojcieszyn, J. W., Schlegel, R. A., Wu, E. S. & Jacobson, K. A. Diffusion of injected macromolecules within the cytoplasm of living cells. *Proc. Natl. Acad. Sci. USA* **78**, 4407–4410 (1981).

24. Arrio-Dupont, M., Foucault, G., Vacher, M., Devaux, P. F. & Cribier, S. Translational diffusion of globular proteins in the cytoplasm of cultured muscle cells. *Biophys. J.* **78**, 901–907 (2000).

25. Verkman, A. S. Solute and macromolecule diffusion in cellular aqueous compartments. *Trends Biochem. Sci.* **27**, 27–33 (2002).

26. Banks, D. S. & Fradin, C. Anomalous diffusion of proteins due to molecular crowding. *Biophys.* **89**, 2960–2971 (2005).

27. Muramatsu, N. & Minton, A. P. Tracer diffusion of globular proteins in concentrated protein solutions. *Proc. Natl. Acad. Sci. USA* **85**, 2984–2988 (1988).

28. Dix, J. A. & Verkman, A. Crowding effects on diffusion in solutions and cells. *Annu. Rev. Biophys.* **37**, 247–263 (2008).

29. Zimmerman, S. B. & Minton, A. P. Macromolecular crowding: Biochemical, biophysical, and physiological consequences. *Annu. Rev. Biophys. Biomol. Struct.* **22**, 27–65 (1993).

30. Mukherjee, S. K., Gautam, S., Biswas, S., Kundu, J. & Chowdhury, P. K. Do macromolecular crowding agents exert only an excluded volume effect? A protein solvation study. *J. Phys. Chem. B* **119**, 14145–14156 (2015).

31. Harada, R., Sugita, Y. & Feig, M. Protein crowding affects hydration structure and dynamics. *J. Am. Chem. Soc.* **134**, 4842–4849 (2012).

32. Cohen, R. D. & Pielak, G. J. A cell is more than the sum of its (dilute) parts: A brief history of quinary structure. *Protein Sci.* **26**, 403–413 (2017).

33. McConkey, E. H. Molecular evolution, intracellular organization, and the quinary structure of proteins. *Proc. Natl. Acad. Sci. USA* **79**, 3236–3240 (1982).

34. Yu, I. et al. Biomolecular interactions modulate macromolecular structure and dynamics in atomistic model of a bacterial cytoplasm. *eLife* **5**, e19274 (2016).

35. Feig, M. & Sugita, Y. Variable interactions between protein crowders and biomolecular solutes are important in understanding cellular crowding. *J. Phys. Chem. B* **116**, 599–605 (2012).

36. Cardinaux, F. et al. Cluster-driven dynamical arrest in concentrated lysozyme solutions. *J. Phys. Chem. B* **115**, 7227–7237 (2011).

37. Kowalczyk, P., Ciach, A., Gauden, P. & Terzyk, A. Equilibrium clusters in concentrated lysozyme protein solutions. *J. Colloid Interface Sci.* **363**, 579–584 (2011).

38. Porcar, L. et al. Formation of the dynamic clusters in concentrated lysozyme protein solutions. *J. Phys. Chem. Lett.* **1**, 126–129 (2010).

39. Liu, Y. et al. Lysozyme protein solution with an intermediate range order structure. *J. Phys. Chem. B* **115**, 7238–7247 (2011).

40. Nawrocki, G., Wang, P.-h, Yu, I., Sugita, Y. & Feig, M. Slow-down in diffusion in crowded protein solutions correlates with transient cluster formation. *J. Phys. Chem. B* **121**, 11072–11084 (2017).

41. Weiss, M., Elsner, M., Kartberg, F. & Nilsson, T. Anomalous subdiffusion is a measure for cytoplasmic crowding in living cells. *Biophys. J.* **87**, 3518–3524 (2004).

42. Guigas, G. & Weiss, M. Sampling the cell with anomalous diffusion—the discovery of slowness. *Biophys. J.* **94**, 90–94 (2008).

43. Meisburger, S. P. et al. Breaking the radiation damage limit with Cryo-SAXS. *Biophys. J.* **104**, 227–236 (2013).

44. Hopkins, J. B. & Thorne, R. E. Quantifying radiation damage in biomolecular small-angle X-ray scattering. *J. Appl. Crystallogr.* **49**, 880–890 (2016).

45. Garman, E. F. & Weik, M. X-ray radiation damage to biological macromolecules: Further insights. *J. Synchrotron. Radiat.* **24**, 1–6 (2017).

46. Kuwamoto, S., Akiyama, S. & Fujisawa, T. Radiation damage to a protein solution, detected by synchrotron X-ray small-angle scattering: Dose-related considerations and suppression by cryoprotectants. *J. Synchrotron. Radiat.* **11**, 462–468 (2004).

47. Young, L. et al. Photon-in/photon-out X-ray free-electron laser studies of radiolysis. *Appl. Sci.* **11**, 701 (2021).

48. Hawkins, C. L. & Davies, M. J. Generation and propagation of radical reactions on proteins. *Biochim. Biophys. Acta Bioenerg.* **1504**, 196–219 (2001).

49. Khalack, J. M. & Lyubartsev, A. P. Solvation structure of hydroxyl radical by car-parrinello molecular dynamics. *J. Phys. Chem. A* **109**, 378–386 (2005).

50. Madsen, A. et al. Materials imaging and dynamics (MID) instrument at the European X-ray free-electron laser facility. *J. Synchrotron. Radiat.* **28**, 637–649 (2021).

51. Da Vela, S. et al. Effective interactions and colloidal stability of bovine γ-globulin in solution. *J. Phys. Chem. B* **121**, 5759–5769 (2017).

52. Girelli, A. et al. Microscopic dynamics of liquid–liquid phase separation and domain coarsening in a protein solution revealed by X-ray photon correlation spectroscopy. *Phys. Rev. Lett.* **126**, 138004 (2021).

53. Allahgholi, A. et al. The adaptive gain integrating pixel detector at the European XFEL. *J. Synchrotron. Radiat.* **26**, 74–82 (2019).

54. Falus, P., Lurio, L. B. & Mochrie, S. G. J. Optimizing the signal-to-noise ratio for X-ray photon correlation spectroscopy. *J. Synchrotron. Radiat.* **13**, 253–259 (2006).

55. Sutton, M., Laaziri, K., Livet, F. & Bley, F. Using coherence to measure two-time correlation functions. *Opt. Express* **11**, 2268 (2003).

56. Cipelletti, L., Bissig, H., Trappe, V., Ballesta, P. & Mazoyer, S. Time-resolved correlation: A new tool for studying temporally heterogeneous dynamics. *J. Phys. Condens. Matter* **15**, S257–S262 (2003).

57. Hruszkewycz, S. O. et al. High contrast X-ray speckle from atomic-scale order in liquids and glasses. *Phys. Rev. Lett.* **109**, 185502 (2012).

58. Begam, N. et al. Kinetics of network formation and heterogeneous dynamics of an egg white gel revealed by coherent X-ray scattering. *Phys. Rev. Lett.* **126**, 098001 (2021).

59. Ruta, B. et al. Wave-vector dependence of the dynamics in supercooled metallic liquids. *Phys. Rev. Lett.* **125**, 055701 (2020).

60. Guo, H. et al. Entanglement-controlled subdiffusion of nanoparticles within concentrated polymer solutions. *Phys. Rev. Lett.* **109**, 055901 (2012).

61. De la Mora, E. et al. Radiation damage and dose limits in serial synchrotron crystallography at cryo- and room temperatures. *Proc. Natl. Acad. Sci. USA* **117**, 4142–4151 (2020).

62. Southworth-Davies, R. J., Medina, M. A., Carmichael, I. & Garman, E. F. Observation of decreased radiation damage at higher dose rates in room temperature protein crystallography. *Structure* **15**, 1531–1541 (2007).

63. Warkentin, M. A., Atakisi, H., Hopkins, J. B., Walko, D. & Thorne, R. E. Lifetimes and spatio-temporal response of protein crystals in intense X-ray microbeams. *IUCrJ* **4**, 785–794 (2017).

64. Schwarz, H. A. Applications of the spur diffusion model to the radiation chemistry of aqueous solutions. *J. Phys. Chem.* **73**, 1928–1937 (1969).

65. Buxton, G. *Radiation Chemistry: Principles and Applications* (Verlag Chemie Publishers, 1987).

66. Attri, P. et al. Generation mechanism of hydroxyl radical species and its lifetime prediction during the plasma-initiated ultraviolet (UV) photolysis. *Sci. Rep.* **5**, 9332 (2015).

67. Baba, K. et al. Quantitative estimation of track segment yields of water radiolysis species under heavy ions around Bragg peak energies using Geant4-DNA. *Sci. Rep.* **11**, 1524 (2021).

68. Northrup, S. H. & Erickson, H. P. Kinetics of protein–protein association explained by Brownian dynamics computer simulation. *Proc. Natl. Acad. Sci. USA* **89**, 3338–3342 (1992).

69. Kubelka, J., Hofrichter, J. & Eaton, W. A. The protein folding 'speed limit'. *Curr. Opin. Struct. Biol.* **14**, 76–88 (2004).

70. Nass, K. Radiation damage in protein crystallography at X-ray free-electron lasers. *Acta Crystallogr. D Struct. Biol.* **75**, 211–218 (2019).

71. Nass, K. et al. Indications of radiation damage in ferredoxin micro-crystals using high-intensity X-FEL beams. *J. Synchrotron. Rad.* **22**, 225–238 (2015).

72. Schlichting, I. Serial femtosecond crystallography: The first five years. *IUCrJ* **2**, 246–255 (2015).

73. Neutze, R., Wouts, R., van der Spoel, D., Weckert, E. & Hajdu, J. Potential for biomolecular imaging with femtosecond X-ray pulses. *Nature* **406**, 752–757 (2000).

74. Chushkin, Y. Deciphering the intrinsic dynamics from the beam-induced atomic motions in oxide glasses. *J. Synchrotron. Radiat.* **27**, 1247–1252 (2020).

75. Ragulskaya, A. et al. Interplay between kinetics and dynamics of liquid-liquid phase separation in a protein solution revealed by coherent X-ray spectroscopy. *J. Phys. Chem. Lett.* **12**, 7085–7090 (2021).

76. Möller, J., Sprung, M., Madsen, A. & Gutt, C. X-ray photon correlation spectroscopy of protein dynamics at nearly diffraction-limited storage rings. *IUCrJ* **6**, 794–803 (2019).

77. Chapman, H. N. et al. Femtosecond X-ray protein nanocrystallography. *Nature* **470**, 73–77 (2011).

78. Hubbell, J. H. & Seltzer, S. M. Tables of X-Ray Mass Attenuation Coefficients and Mass Energy-Absorption Coefficients (version 1.4). [Online] Available: http://physics.nist.gov/xaamdi. (National Institute of Standards and Technology, Gaithersburg, MD, 2004).

Author contributions

F.P., F.Z., F.S., and C.G. conceived the experiment, which was designed and coordinated by M.R., F.P., F.Z., and C.G. A.G. and A.R. prepared and handled the samples. U.B., J.H., J.M., A.R.F., M.S., R.S., A.Z., and A.M. operated MID and collected data together with M.R., A.G., and A.R. M.R., A.G., A.R., F.P., S.T., S.D., M.S.A., M.B., N.B., T.S., and Y.C. performed online data processing and analysis, whereas S.B., H.F.P., M.L.P., M.F., and L.R. were in addition responsible for the elog. M.R. performed offline data processing and analysis. M.R., F.P., F.S., F.Z., and C.G. discussed the XPCS data analysis with input from all authors. R.R. and R.S. supported the development of analysis routines and the integration of experimental equipment. All authors jointly performed the experiment and discussed the final results, to a large extent remotely due to travel restrictions imposed by the COVID-19 pandemic. The manuscript was written by M.R., F.P., and C.G. with input from all authors.

Competing interests

The authors declare no competing interests.

Additional information

Supplementary information The online version contains supplementary material available at https://doi.org/10.1038/s41467-022-33154-7.

Correspondence and requests for materials should be addressed to Mario Reiser, Fivos Perakis or Christian Gutt.

Peer review information *Nature Communications* thanks the anonymous reviewer(s) for their contribution to the peer review of this work.

Reprints and permission information is available at http://www.nature.com/reprints

Publisher's note Springer Nature remains neutral with regard to jurisdictional claims in published maps and institutional affiliations.